is, we observe electron spins rather than hole spins. The latter has been assumed in a number of spin precession measurements on zinc blende semiconductors[3–5], and we believe that these data provide direct evidence that Faraday-rotation measurements are truly selective in measuring electron spins. We do not observe any spin polarization travelling oppositely to the electron spins, so the assumption that hole spins scatter rapidly in these systems appears to be valid[5,6]. In the insulating (undoped) control sample, no changes in spin profile are observed at fields up to 400 V cm^{-1}.

To obtain a more precise measurement of spin drift in these systems, we note that each constituent of the spin resonance has a different periodicity, $g\mu_B(\Delta t + nt_{rep})/\hbar$, in the applied magnetic field, B. Thus, by varying B at each displacement, we can separately identify the spatial extent of the various $\mathbf{m}_n$ by Fourier decomposition. Figure 2a shows the Faraday rotation versus magnetic field profile taken at a displacement of $\Delta x = 54\,\mu$m from the injection point and a pump–probe delay of $\Delta t = -10$ ps. An applied electric field of -37 V cm^{-1} creates a measurable spin polarization at this lateral position, and harmonic analysis (Fig. 2a inset) reveals that the oscillatory behaviour arises from Larmor precession of the third, fourth and fifth most recent pump pulses. By obtaining field scans over a range in Δx, we may track the spatial position of successive spin packets, as indexed by their injection time. Figure 2b shows a two-dimensional assembly of field scans similar to Fig. 2a, taken from $\Delta x = -54\,\mu$m to $+137\,\mu$m. A narrowing of the spin resonances and an increasing periodicity in field accompanies lateral displacement, reflecting increased pulse ages with increased Δx. Figure 2b inset shows the corresponding harmonic power versus position, showing that pulse ages increase in steps of t_{rep}. The data can thus be used to mark the positions of individual spin packets, and indicate that spin drift is linear in time and corresponds to a drift mobility $\mu_d = 3 \times 10^3$ cm^2 V^{-1} s^{-1}.

By explicitly fitting the oscillatory data to obtain the amplitude of each spin packet at every position, we compare the profiles of the ten most recent spin injections at zero and -37 V cm^{-1} in Fig. 2c, where the former are laterally displaced for clarity. These data provide a quantitative measure of spin drift and diffusion over a 130-ns interval following spin injection. To remove artefacts from a strongly field-dependent transverse spin lifetime in the zero-bias sample, these data are obtained by fitting only the $B = 0$ T spin resonance. As seen on the logarithmic amplitude scale, the zero-bias spins decay exponentially with a characteristic time $T_2^* = 29$ ns. By fitting the broadening of the spin packet to $\sqrt{D_s(t + t_o)}$, where $t = \Delta t + nt_{rep}$ is the age of the nth pulse and t_o adjusts for its initial width, we obtain a spin diffusion constant D_s that exceeds the electron diffusion constant, $D_e = \mu_d kT/e$, by more than one order of magnitude. This discrepancy suggests that spin diffusion here involves both electron and pure spin diffusion. Applying a voltage does not introduce any severe decoherence ($T_2^* \sim 17$ ns) and produces a more dramatic profile distortion during transport.

A more subtle effect is a suppression of the $B = 0$ T spin motion in this sample. Though difficult to distinguish within the colour scale of Fig. 2b, a relative dip in spin polarization appears for $\Delta x \neq 0$ and fields below a few gauss, as seen in Fig. 2a. Figure 3a–e shows that these effects become stronger in the thinner sample where, as the electric field is increased from 0 to -92.5 V cm^{-1}, the $B = 0$ T resonance disappears completely and is eventually replaced by neighbouring resonances. These data suggest that electric current flow generates an additional internal magnetic field, B_{int}, that dominates near zero external magnetic field. Figure 3g shows a cross-section of the most recent spin packet, separated from other spins by an electric field of -92.5 V cm^{-1}. The data deviate from an expected cosinusoidal behaviour and are more accurately described by an effective field strength, $B_{eff}{}^2 = B_{int}{}^2 + B^2$, with $B_{int} = 0.023$ T. A change in the effective magnetic field within the profile of each packet is evident from the shift of the resonances to lower field strengths at larger displacements. This behaviour cannot be explained by a variation of g-factors throughout the profile of the spin packet because the Larmor frequency at larger magnetic fields is independent of Δx (not shown). Hence by fitting the field dependence of the Faraday rotation at different Δx, we obtain a profile of the internal magnetic field strength throughout the most recent pulse (Fig. 3f, top). This field distribution leads to inhomogeneous dephasing of the spin direction within each spin packet and scales linearly with the electric field. Similar fits for the thicker sample indicate an internal field that is two orders of magnitude smaller.

Although the magnetic field generated by electric current is of the correct geometry (Fig. 3f, bottom), it changes sign in passing from the front to the back face of the sample whereas the data are well fitted by a single internal field at each Δx. Moreover, for uniform current flow the field strength should scale linearly with the thickness of the sample, while the opposite trend is observed in our data; rough estimates of the surface field strength give the correct order of magnitude for the thicker sample but fail for the thinner sample. One possible explanation is that the optical injection creates a significantly non-uniform, and perhaps filamentary, current flow[7]. Further consideration must also be given to the inherent spin splitting that is known to occur in the conduction band of GaAs away from zero wavevector[8]. We find it difficult to identify B_{int} solely with the corresponding effective field, however, as the latter is linearly proportional to and uniquely determined by the drift velocity[8] whereas the former is dramatically different in thick and thin samples with the same drift velocity. □

Received 4 August; accepted 5 November 1998.

1. Prinz, G. Spin-polarized transport. *Phys. Today* **48,** 58–63 (1995).
2. Kane, B. E. A silicon based nuclear spin quantum computer. *Nature* **393,** 133–137 (1998).
3. Kikkawa, J. M. & Awschalom, D. D. Resonant spin amplification in GaAs. *Phys. Rev. Lett.* **80,** 4313–4316 (1998).
4. Kikkawa, J. M., Smorchkova, I. P., Samarth, N. & Awschalom, D. D. Room-temperature spin memory in two-dimensional electron gases. *Science* **277,** 1284–1287 (1997).
5. Worsley, R. E., Traynor, N. J., Grevatt, T. & Harley, R. T. Transient linear birefringence in GaAs quantum wells. *Phys. Rev. Lett.* **76,** 3224–3227 (1996).
6. Oestreich, M. *et al.* Temperature and density dependence of the electron Landé g-factor in semiconductors. *Phys. Rev. B* **53,** 7911–7916 (1996).
7. Niedernostheide, F.-J., Hirschinger, J., Prettl, W., Novak, V. & Kostial, H. Oscillations of current filaments in n-GaAs caused by a magnetic field. *Phys. Rev. B* **58,** 4454–4458 (1998).
8. Kalevich, V. K. & Korenov, V. L. Effect of electric field on the optical orientation of 2D electrons. *Pis'ma Zh. Eksp. Teor. Fiz.* **52,** 230–235 (1990) [*JETP Lett*. **52,** 230–235 (1990)].

Acknowledgements. We thank S. J. Allen for discussions and acknowledge support from the ARO and NSF QUEST STC.

Correspondence and requests for materials should be addressed to D.D.A. (e-mail: awsch@physics.ucsb.edu).

Entropic trapping of macromolecules by mesoscopic periodic voids in a polymer hydrogel

Lei Liu*†, Pusheng Li*† & Sanford A. Asher*

* *Department of Chemistry, University of Pittsburgh, Pittsburgh, Pennsylvania 15260, USA*

The separation of macromolecules such as polymers and DNA by means of electrophoresis, gel permeation chromatography or filtration exploits size-dependent differences in the time it takes for the molecules to migrate through a random porous network. Transport through the gel matrices, which usually consist of full swollen crosslinked polymers[1–11], depends on the relative size of

† Present address: Praxair Service Technologies Inc., 1555 Main St, Indianapolis, Indiana 46254, USA (L.L.); Epsilon Inc., HPOS, 50 Cambridge St, Burlington, Massachusetts 01803, USA (P.L.).

the macromolecule compared with the pore radius. Sufficiently small molecules are thought to adopt an approximately spherical conformation when diffusing through the gel matrix[1], whereas larger ones are forced to migrate in a snake-like fashion[3–5]. Molecules of intermediate size, however, can get temporarily trapped in the largest pores of the matrix, where the molecule can extend and thus maximize its conformational entropy. This 'entropic trapping' is thought to increase the dependence of diffusion rate on molecular size[6–16]. Here we report the direct experimental verification of this phenomenon. Bragg diffraction from a hydrogel containing a periodic array of monodisperse water voids confirms that polymers of different weights partition between the hydrogel matrix and the water voids according to the predictions of the entropic trapping theory. Our approach might also lead to the design of improved separation media based on entropic trapping.

Figure 1 illustrates the fabrication of a polymerized crystalline colloidal array (CCA) of spherical water voids. An aqueous suspension of ~100-nm-diameter monodisperse silica spheres was induced to self-assemble into a three-dimensional CCA by removing the ionic impurities from the medium with ion-exchange resin. This self-assembly, driven by interparticle electrostatic repulsion due to negative particle surface charges, minimizes the total system energy[17–24]. The array adopts either a body-centred cubic or face-centred cubic structure[17–24]. Similar to atomic crystals diffracting X-rays, CCAs Bragg-diffract light in the near-infrared to near-ultraviolet spectral regions, depending on the interparticle spacing and the system refractive index[17,21–24].

We immobilized the CCA in a polyacrylamide hydrogen network[21–24], by mixing acrylamide, *N*,*N*′-methylene-bisacrylamide, and photo-initiator 2,2-diethoxyacetophenone into the silica CCA dispersion. Photo-polymerization results in a ~100-μm-thick hydrogel film, where the silica spheres are locked in their cubic lattice. These polymerized CCA hydrogel films contain a high polymer and crosslinker content, and are sufficiently robust to allow further chemical modification. This silica polymerized CCA was used as a template to create a polymerized CCA of ~100-nm-diameter spherical water voids (HPCCA) by hydrofluoric acid etching. Both diffraction and gravimetry demonstrate complete removal of the silica colloids with little effect on the hydrogel network.

We soaked the HPCCA film in deionized water solutions of sodium polystyrene sulphonate (NaPSS) of different molecular masses with narrow molecular-mass distributions ($M_w/M_n \approx 1.1$, where M_w and M_n are the mass-average and number-average molecular masses) for 3–10 days until equilibrium was established. Figure 2 shows the experimental method and the measured HPCCA diffraction spectra before and after soaking in NaPSS solution.

We model the CCA Bragg diffraction by combining dynamical diffraction and light scattering theory[23–26], and analyse the diffracted wavelength and intensity changes to sensitively probe the chemical composition in the voids and in the gel medium. Both the diffraction intensity (I_D) and wavelength (λ_D) depend upon the refractive indices[23–26]:

$$-\log\left(\frac{I_T}{I_0}\right) = -\log\left(1-\frac{I_D}{I_0}\right) = f(n_{void}, n_{gel}, n_{crystal}) \quad (1)$$

$$\lambda_D = g(n_{crystal}, n_{gel}) \quad (2)$$

where I_T and I_0 are the transmitted and incident light intensities. The refractive indices are related to the chemical compositions by:

$$n_{void} = n_{water}(1 - C_H) + n_{PSS}C_H \quad (3)$$

$$n_{gel} = n_{AMD}\phi_a + (1-\phi_a)[n_{water}(1-C_G) + n_{PSS}C_G] \quad (4)$$

$$n_{crystal} = n_{gel}(1-\phi_{void}) + n_{void}\phi_{void} \quad (5)$$

where n_{water}, n_{AMD}, and n_{PSS} represent the refractive indices of water, polyacrylamide and NaPSS, respectively, ϕ_{void} is the volume fraction of the voids in the whole system, ϕ_a is the volume fraction of the polyacrylamide network in the gel medium, C_H and C_G are the NaPSS concentrations (in wt%) in the voids and in the gel medium. C_G here is normalized with respect to only the total solution volume of the interstitial gel medium; the polyacrylamide chain network is excluded.

More uptake of NaPSS in the voids than in the gel medium decreases the refractive-index difference between the voids and the gel medium, which decreases the diffraction intensity. Uptake of NaPSS also increases the overall crystal refractive index, and slightly red-shifts the diffracted wavelength.

Figure 3a shows the dependence of the measured NaPSS partition coefficient K_{HG} ($=C_H/C_G$) on the NaPSS molecular mass. The natural logarithm of K_{HG} initially increases almost linearly with NaPSS molecular mass and then levels off. For the highest molecular masses, C_H is ~4 times larger than that in the gel medium.

The observed dependence of K_{HG} on the molecular mass of NaPSS must result from entropic effects because enthalpic interactions between the NaPSS chains and the hydrogel network should show little molecular mass dependence. The embedded voids possess essentially the same chemical properties as the rest of the gel medium except that the diameter of the voids (~100 nm) is much larger than the mean pore diameter of the gel network (pore diameter is in the nanometre size range; ref. 27). Large flexible NaPSS chains preferentially partition into the voids in order to maximize their conformational entropy.

When the configuration of a flexible chain polymer is treated using self-avoiding random-walk statistics, the constrained conformational entropy in a box of a particular shape can be calculated[13,14,28–30]. The entropy dominated partition coefficient K_{ij}

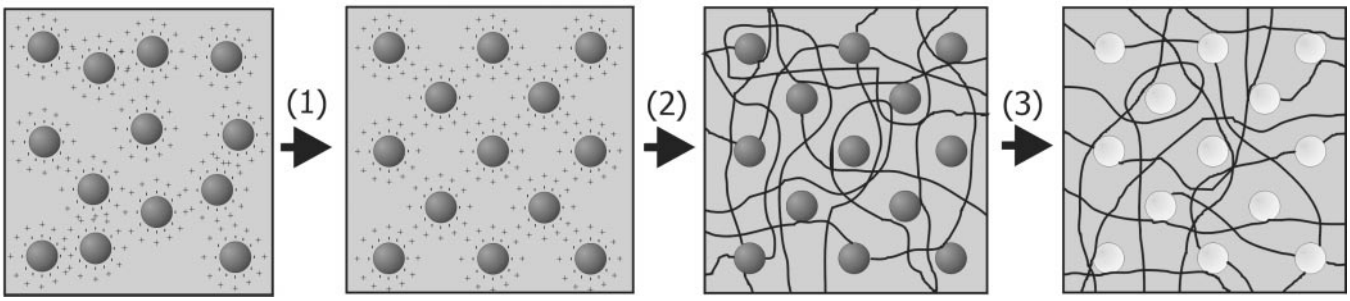

Figure 1 Fabrication of hydrogel with a cubic array of spherical water voids. (1), Monodisperse silica spheres electrostatically self-assemble into a crystalline colloidal array (CCA) in aqueous solution. (2), The silica CCA is immobilized within a random polyacrylamide hydrogel network matrix (a polymerized CCA). (3), Silica spheres are etched out with hydrofluoric acid to result in a polymerized CCA of water voids (HPCCA).

between two confining cavities i and j will scale as:

$$-\ln K_{ij} = -\ln\left(\frac{C_i}{C_j}\right) \approx N\left[\left(\frac{1}{R_i}\right)^{\frac{1}{\upsilon}} - \left(\frac{1}{R_j}\right)^{\frac{1}{\upsilon}}\right] \quad (6)$$

where C_i and C_j are the monomer concentrations in cavities i and j, respectively, N is the polymer molecular mass, υ is the Flory universal exponent, and R_i and R_j are the characteristic radii of cavities i and j. This thermodynamic model assumes well-defined rigid boundary conditions, and is only valid for cavities sufficiently large to accommodate the entire polymer chain[13,14,28].

At low molecular mass, our results agree qualitatively with these predictions. When the pore sizes of both the voids and the gel network are much larger than the NaPSS molecular sizes, there is little constraint in either region; no partitioning occurs. As the molecular mass increases, $\ln K_{HG}$ increases linearly with molecular mass as predicted by entropic trapping theory.

But at the highest molecular masses, this linear relationship fails, presumably because the theory is based on impermeable rigid boundaries and the assumption that a single cavity contains the entire polymer chain. In the hydrogel matrix, the 'boundaries' of the 'cavities' are poorly defined because the aqueous solution forms a continuous phase interwoven in a three-dimensional fashion with the crosslinked polyacrylamide chains. When the NaPSS molecular size is much larger than the mean mesh spacing of the gel medium, the chain will simultaneously occupy two or more adjacent pores of that medium. Each section will behave like an independent polymer chain of smaller molecular mass. As predicted by Muthukumar *et al.*[13,14], this effect will diminish the molecular-mass dependence of entropic trapping and the effective size of the hydrogel pores (R_j) will appear to increase with the NaPSS molecular mass (equation (6)).

Entropic trapping also depends on concentration. Figure 3b shows the dependence of K_{HG} on the NaPSS reservoir solution concentration (C_S) for NaPSS with the largest molecular mass (1.2×10^6 dalton, radius of gyration $R_g \approx 34$ nm) and the smallest (1.6×10^3 dalton). For the lowest molecular mass, K_{HG} slightly increases monotonically with C_S. In contrast, for the highest molecular mass, K_{HG} sharply increases until it reaches a maximum at ~5% C_S, and then decreases as C_S increases further.

The observed concentration dependence of K_{HG} may result from NaPSS intermolecular interactions such as exclusion and entanglement[2]. When polymer chains enter a cavity, they will encounter intermolecular exclusion from volumes already occupied by other polymer chains. The effective cavity volume will decrease as polymer chains enter. As exclusion is more effective in the hydrogel pores than in the voids, K_{HG} should in general increase with concentration. The more rapid initial increase of K_{HG} with C_S seen for the higher molecular mass NaPSS chains may be due to the fact that polymer chains of higher molecular mass possess larger hydrodynamic volumes than those of lower mass. At identical concentrations, larger polymer chains thus exclude each other more effectively than smaller chains.

However, an increase in K_{HG} causes an increasing concentration difference between the voids and the gel medium, thus exaggerating volume exclusion effects in the voids at higher NaPSS concentrations. In the case of the highest molecular mass NaPSS, the solution concentration in the voids may be sufficiently high to cause entanglement, while the gel medium remains in the dilute solution regime. As pointed out by Guillot *et al.*[6], both effects counteract entropic trapping from the hydrogel network and could eventually result in a decrease of K_{HG} with C_S.

We expect that the fabrication approach we have used in this study could serve as a general motif to design new separation materials in which macromolecules could be retarded, trapped and separated. Such materials might also be useful as specific biochemical trapping materials for applications in drug delivery

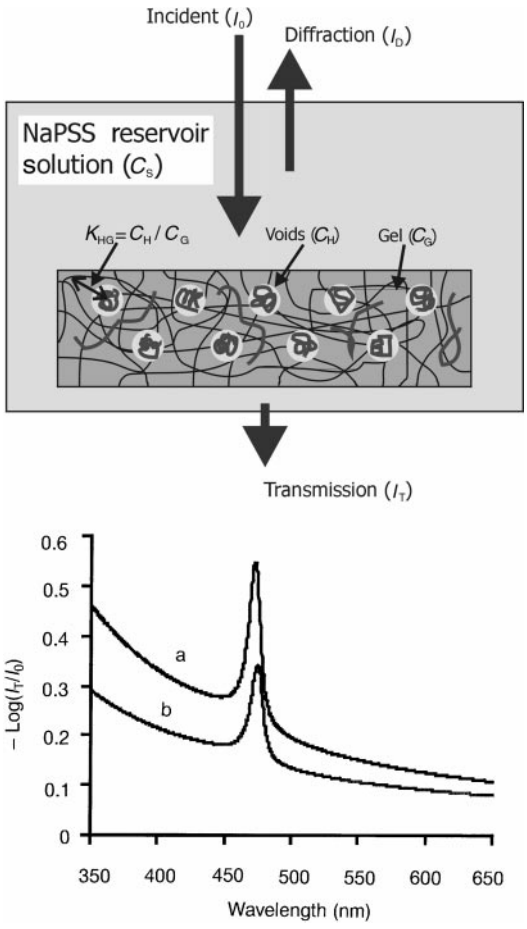

Figure 2 Bragg diffraction probes the chemical composition of HPCCA. Top, Experimental setup. Bottom, measured Bragg diffraction spectra from HPCCA film before (trace a) and after (trace b) exchange with a NaPSS reservoir solution.

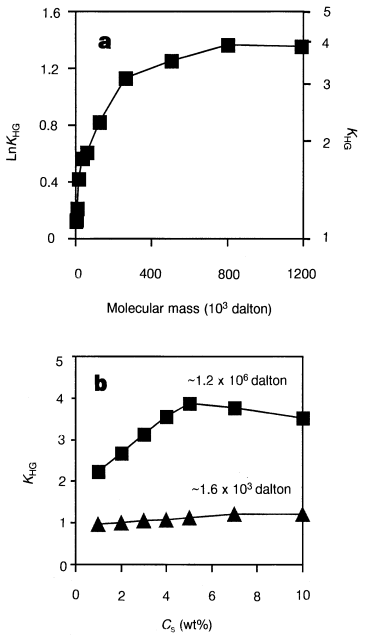

Figure 3 Dependence of NaPSS partitioning on molecular mass and concentration. Dependence of the NaPSS partition coefficient, K_{HG} ($=C_H/C_G$), between the voids and the gel medium on: **a**, the molecular mass at 5 wt% reservoir concentration, and **b**, the reservoir concentration (C_S). The standard deviation in the partition coefficient is likely to be significantly smaller than the size of the data points.

and controlled-release processes, or as semi-homogeneous microreactors for applications in organic, bioengineering and combinatorial synthesis. In these applications, Bragg diffraction from the arrays could be used to probe the existence and location of chemical species as a means to monitor physiochemical processes in real time. □

Received 23 April; accepted 11 September 1998.

1. Rodbard, D. & Chrambach, A. Unified theory for gel electrophoresis and gel filtration. *Proc. Natl. Acad. Sci. USA* **65,** 970–977 (1970).
2. Teraoka, I. Interferometric study of transition from weak to strong penetration of a polymer solution into a porous silica bead. *Macromolecules* **29,** 2430–2439 (1996).
3. Lerman, L. S. & Frisch, H. L. Why does the electrophoretic mobility of DNA in gels vary with the length of the molecule? *Biopolymers* **21,** 995–997 (1982).
4. Lumpkin, O. J., Dejardin, P. & Zimm, B. H. Theory of gel electrophoresis of DNA. *Biopolymers* **24,** 1573–1593 (1985).
5. Slater, G. W. & Noolandi, J. On the reptation theory of gel electrophoresis. *Biopolymers* **25,** 431–454 (1986).
6. Guillot, G., Leger, L. & Rondelez, F. Diffusion of large flexible polymer chains through model porous membranes. *Macromolecules* **18,** 2531–2537 (1985).
7. Rotstein, N. A. & Lodge, T. P. Tracer diffusion of linear polystyrenes in poly(vinyl methyl ether) gels. *Macromolecules* **25,** 1316–1325 (1992).
8. Smisek, D. L. & Hoagland, D. A. Electrophoresis of flexible macromolecules: evidence for a new mode of transport in gels. *Science* **248,** 1221–1223 (1990).
9. Muthukumar, M. & Hoagland, D. A. Evidence for entropic barrier transport of linear, star, and ring macromolecules in electrophoresis gels. *Macromolecules* **25,** 6696–6698 (1992).
10. Rousseau, J., Drouin, G. & Slater, G. W. Entropic trapping of DNA during gel electrophoresis: effect of field intensity and gel concentration. *Phys. Rev. Lett.* **79,** 1945–1948 (1997).
11. Noolandi, J., Rousseau, J. & Slater, G. W. Self-trapping and anomalous dispersion of DNA in electrophoresis. *Phys. Rev. Lett.* **58,** 2428–2431 (1987).
12. Slater, G. W. & Wu, S. Y. Reptation, entropic trapping, percolation, and Rouse dynamics of polymers in "random" environments. *Phys. Rev. Lett.* **75,** 164–167 (1995).
13. Baumgärtner, A. & Muthukumar, M. A trapped polymer chain in random porous media. *J. Chem. Phys.* **87,** 3082–3088 (1987).
14. Muthukumar, M. & Baumgärtner, A. Effects of entropic barriers on polymer dynamics. *Macromolecules* **22,** 1937–1941 (1989).
15. Kim, H., Chang, T., Yohanan, J. M., Wang, L. & Yu, H. Polymer diffusion in linear matrices: polystyrene in toluene. *Macromolecules* **19,** 2737–2744 (1986).
16. Nemoto, N., Kishine, M., Inoue, T. & Osaki, K. Tracer diffusion of linear polystyrene in entanglement networks. *Macromolecules* **23,** 659–664 (1990).
17. Hiltner, P. A. & Krieger, I. M. Diffraction of light by ordered suspensions. *J. Phys. Chem.* **73,** 2386–2389 (1969).
18. Clark, N. A., Hurd, A. J. & Ackerson, B. J. Single colloidal crystals. *Nature* **281,** 57–60 (1979).
19. Kesavamoorthy, R., Tandon, S., Xu, S., Jagannathan, S. & Asher, S. A. Self-assembly and ordering of electrostatically stabilized silica suspensions. *J. Colloid Interface Sci.* **153,** 188–198 (1992).
20. Asher, S. A. Crystalline narrow band radiation filter. US Patent Nos 4,627,689 and 4,632,517 (1986).
21. Weissman, J. M., Sunkara, H. B., Tse, A. S. & Asher, S. A. Thermally switchable periodicities and diffraction from mesoscopically ordered materials. *Science* **274,** 959–960 (1996).
22. Holtz, J. H. & Asher, S. A. Polymerized colloidal crystal hydrogel films as intelligent chemical sensing materials. *Nature* **389,** 829–832 (1997).
23. Rundquist, P. A., Photinos, P., Jagannathan, S. & Asher, S. A. Dynamical Bragg diffraction from crystalline colloidal arrays. *J. Chem. Phys.* **91,** 4932–4941 (1989).
24. Liu, L., Li, P. & Asher, S. a. Fortuitously superimposed lattice plane secondary diffraction from crystalline colloidal arrays. *J. Am. Chem. Soc.* **119,** 2729–2732 (1997).
25. Zachariasen, W. H. *Theory of X-ray Diffraction in Crystals* (Dover, New York, 1957).
26. Van de Hulst, H. C. *Light Scattering by Small Particles* (Dover, New York, 1957).
27. Righetti, P. G. Macroporous gels: facts and misfacts. *J. Chromatogr. A* **698,** 3–17 (1995).
28. Casassa, E. F. Equilibrium distribution of flexible polymer chains between a macroscopic solution phase and small voids. *Polymer Lett.* **5,** 773–778 (1967).
29. Flory, P. J. *Principles of Polymer Chemistry* (Ithaca, New York, 1953).
30. De Gennes, P. G. *Scaling Concepts in Polymer Physics* (Ithaca, New York, 1979).

Acknowledgements. We thank M. D. Morris, D. Pine, J. Holtz, J. M. Weissman and G. Pan for discussions. This work was supported by the Office of Naval Research and the US National Science Foundation.

Correspondence and requests for materials should be addressed to S.A.A. (e-mail: asher+@pitt.edu).

A nanomechanical device based on the B–Z transition of DNA

Chengde Mao, Weiqiong Sun, Zhiyong Shen & Nadrian C. Seeman

Department of Chemistry, New York University, New York, New York 10003, USA

The assembly of synthetic, controllable molecular mechanical systems[1–7] is one of the goals of nanotechnology. Protein-based molecular machines, often driven by an energy source such as ATP, are abundant in biology[8,9]. It has been shown previously that branched motifs of DNA can provide components for the assembly of nanoscale objects[10], links[11] and arrays[12]. Here we show that such structures can also provide the basis for dynamic assemblies: switchable molecular machines. We have constructed a supramolecular device consisting of two rigid DNA 'double-crossover' (DX) molecules connected by 4.5 double-helical turns. One domain of each DX molecule is attached to the connecting helix. To effect switchable motion in this assembly, we use the transition between the B and Z[13,14] forms of DNA. In conditions that favour B-DNA, the two unconnected domains of the DX molecules lie on the same side of the central helix. In Z-DNA-promoting conditions, however, these domains switch to opposite sides of the helix. This relative repositioning is detected by means of fluorescence resonance energy transfer spectroscopy, which measures the relative proximity of two dye molecules attached to the free ends of the DX molecules. The switching event induces atomic displacements of 20–60 Å.

It has been recognized for a long time that the B–Z transition could be used to drive a DNA-based mechanical device[15], but the development of such a device required the discovery of a rigid DNA motif to provide a fixed level arm: the rigidity of the DX molecule[16] is the key element that enables the construction of this device.

A molecular model of the system is shown at the top of Fig. 1. A long central helix is flanked on either end by two 'DAO' molecules, where DAO (for double-crossover, antiparallel, odd-number) means that this is a DNA double-crossover molecule whose helices are antiparallel to each other, and whose crossover points are separated by an odd number (three) of double helical half-turns[17]. The ends of all helices have been closed with dT_4 hairpin loops (made up of four deoxythymidines); consequently, the entire construct consists of three cyclic strands of DNA, the two blue strands on the ends, and the red strand that contains a yellow central

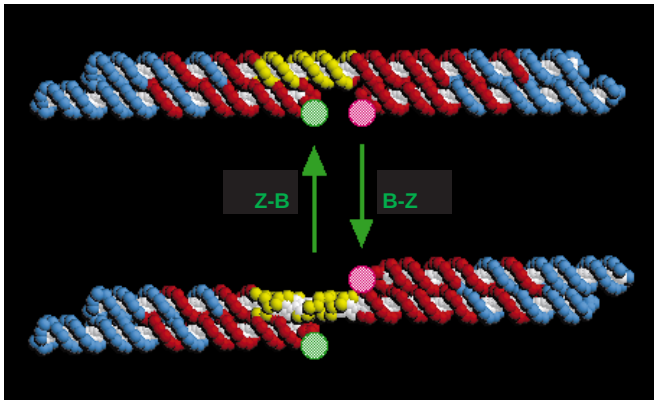

Figure 1 Design of the nanomechanical device. The device consists of two DNA double crossover (DX) molecules with the DAO motif[17] connected by 4.5 turns of DNA between the nearest crossover points. Top, molecular model of the molecule constructed entirely from right-handed B-DNA. Each nucleotide is shown as two spheres, a coloured one for the backbone and a white one for the base. Three cyclic strands are shown, one in the centre drawn as a red strand with a central yellow segment, and two blue strands on the ends that are each triply catenated to the red strand. Fluorescent dyes are drawn schematically as stippled green (fluorescein) and magenta (Cy3) circles attached to the free hairpins near the middle of the molecule. At the centre of the connecting helix is a 20-nucleotide region of proto-Z DNA in the B-DNA conformation, shown in yellow. When the B–Z transition takes place, this same yellow portion becomes left-handed Z-DNA (bottom). When the transition occurs, the two DX molecules change their relative positions, increasing the separation of the dyes. It is possible to cycle this system in both directions.